Structure of the thermal boundary layer for turbulent Rayleigh-Bénard convection of air in a long rectangular enclosure

Anna Maystrenko, Christian Resagk, and André Thess
Department of Mechanical Engineering, Ilmenau University of Technology, P.O. Box 100565, 98684 Ilmenau, Germany
(Received 5 December 2006; published 6 June 2007)

Measurements of the temperature distribution were performed in the upper (cold) boundary layer of a rectangular Rayleigh-Bénard cell with aspect ratios $\Gamma_x=5$ and $\Gamma_y=1$ using air with Prandtl number Pr=0.71 as the working fluid. The range of investigated Rayleigh numbers was from $\mathrm{Ra}\approx 6\times 10^7$ to $\mathrm{Ra}\approx 6\times 10^8$, and the measurements were taken at two different positions with the purpose of understanding the variation of the properties of the thermal boundary layer along the cell. We present profiles of the mean temperature, rms temperature fluctuations, skewness, and kurtosis as a function of the distance from the cooling plate from which we extract scaling exponents and boundary layer thicknesses. Whereas most of these quantities are found to depend monotonically on the Rayleigh number for the peripheral measurement position, their values at the central measurement position exhibit a high degree of variability. These observations indicate that the properties of the thermal boundary layer in large-aspect-ratio convection can have strong spatial variations.

DOI: 10.1103/PhysRevE.75.066303 PACS number(s): 47.27.te

I. INTRODUCTION

The Rayleigh-Bénard experiment is an interesting model for the study of turbulence and heat transport whose global properties such as the Nusselt number as a function of the Rayleigh number have been investigated in great detail in the past [1–3]. There are much fewer local measurements within the thermal boundary layer [4–9], and those measurements which exist either had a moderate spatial resolution [6,8,9] or were performed at aspect ratios of order 1 [5]. The purpose of this paper is to fill this gap by studying the properties of a turbulent boundary in a large-aspect-ratio cell.

Rayleigh-Bénard convection occurs in a volume that is heated from below with the temperature T_h and cooled from above with temperature T_c. There is hence a temperature difference $\Delta T=T_h-T_c$ between the two plates, which drives the flow. The boundary conditions are usually assumed as adiabatic at the sidewalls and isothermal at the top and bottom plates. When this kind of convection takes place in a rectangular volume, it can be described in detail by four control parameters, namely, the Rayleigh number Ra, the Prandtl number Pr, and the two aspect ratios Γ_x and Γ_y. The Rayleigh and Prandtl numbers are defined as

$$\mathrm{Ra}=\frac{\beta g\Delta T h^3}{\nu\kappa},\quad \mathrm{Pr}=\frac{\nu}{\kappa}. \tag{1}$$

whereas the aspect ratios are given by

$$\Gamma_x=\frac{l}{h},\quad \Gamma_y=\frac{w}{h}. \tag{2}$$

In the given equations we used the following variables: β is the coefficient of thermal expansion, g is the acceleration of gravity, h is the distance between heating and cooling plates, l is the length of the cell, w is the width of the cell, ν is the kinematic viscosity, and κ is the thermal diffusivity. When the value of Ra is above 10^6, the so-called turbulent convection regime in air occurs [10]. The concept of "hard turbulence," which has been studied in previous works [11], predicts a transition from soft to hard turbulence at $\mathrm{Ra}=4\times 10^7$. Since our Ra range begins at 6×10^7 we are in the regime of hard turbulence and do not observe the transition from soft to hard turbulence. It was also generally observed that large-scale circulations in Rayleigh-Bénard convection exist above $\mathrm{Ra}=5\times 10^7$ [12]. This regime is the focus of our paper.

The goal of the present work is to investigate the variability of the thermal boundary layer in air in a Rayleigh-Bénard experiment with two different aspect ratios, a large one and one of order unity. More precisely, we use a rectangular convection cell with one large aspect ratio, namely, $\Gamma_x=5$, and one intermediate aspect ratio $\Gamma_y=1$. We are interested in the structure of the temperature field in the region below the cooling plate, which is referred to as the thermal boundary layer. Our particular concern is to compare the vertical structure of the thermal boundary layer at two distant locations. The motivation for such an investigation is twofold.

First, it is known that in Rayleigh-Bénard experiments with $\Gamma_x\approx\Gamma_y\approx 1$ a robust large-scale circulation exists which is sometimes called "wind" and that the properties of the thermal boundary layer change along this wind [5,14]. By contrast, there is no permanent large-scale structure when the aspect ratio is large [7], and it is therefore interesting to analyze how strongly the structure of the thermal boundary layer depends on the horizontal position. A second motivation for studying Rayleigh-Bénard convection in a cell with vastly different aspect ratios comes from the fact that the reliable prediction of air flow in passenger compartments of airplanes, trains, and buses requires a comprehensive understanding of the properties of large-scale coherent structures in mixed (forced and thermal) convection. Understanding pure thermal convection, as in the present work, is a prerequisite to accomplish this task. Before describing our experiment and results in detail we briefly recall some basic features and open questions regarding the behavior of the mean temperature profiles $T(z)$ in Rayleigh-Bénard convection (where z denotes the distance from the cooling plate).

The primary quantity necessary to nondimensionalize the temperature profiles is the kinematic heat flux q, which is

 ©2007 The American Physical Society

related to the temperature gradient at the wall as

$$q = \kappa \left. \frac{\partial T}{\partial z} \right|_{z=0}. \tag{3}$$

The kinematic heat flux defines a natural scale of temperature variations within the thermal boundary layer, which we denote by

$$T_q = \left(\frac{q^3}{\beta g \kappa} \right)^{1/4}, \tag{4}$$

and which constitutes the thermal analog to the friction velocity in turbulent shear flows. This temperature scale has been used since the very early work on thermal convection [9,13] and has recently been successfully applied by [15] to represent temperature profiles in vertical heated walls. T_q together with q define a length scale

$$\delta = \frac{\kappa T_q}{q} = \left(\frac{\kappa^3}{\beta g q} \right)^{1/4}, \tag{5}$$

which is the microscale of our problem. Following the procedure known from shear flows we introduce the nondimensional temperature Θ^+ and length z^+ via

$$\Theta^+ = \frac{T - T_c}{T_q}, \quad z^+ = \frac{z}{\delta}. \tag{6}$$

For sufficiently high Rayleigh numbers it can be assumed that there is a range of length scales z which are much larger than the "inner" length scale δ and much smaller than the "outer" length scale h in which the temperature profile has a universal shape.

The earliest phenomenological theory of turbulent convection which goes back to Prandtl [16] assumes that the difference between the temperature $T(z)$ and the temperature T_b far away from the plate (called the bulk temperature) should be independent of the molecular transport coefficients κ and ν. On dimensional grounds, the only combination that satisfies this condition is

$$T(z) - T_b = A \left(\frac{q^2}{\beta g z} \right)^{1/3}, \tag{7}$$

where A is a phenomenological coefficient that has to be determined from experiments. Using the above definition of nondimensional quantities together with $T_b = T_c + \Delta T/2$ and the definition of the Nusselt number $\mathrm{Nu} = qh/\kappa \Delta T$, we can write this profile as

$$\Theta^+ = \frac{A}{z^{+1/3}} + B \tag{8}$$

with $B = \mathrm{Ra}^{1/4}\mathrm{Pr}^{1/4}/2\mathrm{Nu}^{3/4}$. An alternative is to assume that the temperature gradient is independent of the outer length scale h, which leads to the classical logarithmic scaling law [15,17,22]

$$\Theta^+ = C \ln(z^+) + D. \tag{9}$$

There is an ongoing and still unresolved debate in the turbulent shear flow community as to whether the mean velocity in pipe and channel flows can be equally well represented using a power law scaling [18–20]. In line with these arguments one should also consider the possibility of a power law temperature scaling of the form

$$\Theta^+ = E z^{+\alpha}. \tag{10}$$

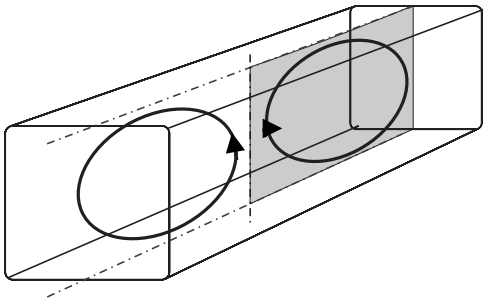

FIG. 1. Schematic geometry of the Rayleigh-Bénard cell used in the present work together with flow pattern observed at $\mathrm{Ra} = 6 \times 10^8$ in a preliminary flow visualization study using a light-sheet technique.

One of the purposes of our paper is to understand which of these scaling laws is realized in turbulent Rayleigh-Bénard convection. The representation of temperature profiles in wall variables requires a knowledge of the heat flux. Since we do not have direct access to this quantity, we will not represent our measurements in terms of Θ^+ and z^+ but rather in outer units, namely, ΔT and h. However, we will briefly return to this question in the last section.

The main purpose of the present experimental study was to characterize the temperature distribution in the cell by means of local temperature measurement at two lateral positions under the cooling plate. Since the temperature behavior is connected directly with the flow structure in the cell, a preliminary flow visualization experiment was performed in order to select those measurement positions which would provide a maximum of information about the large-scale circulation. It is generally known that for a rectangular channel that is quite long compared to its width, the time-averaged coherent structures have the shape of short cylinders with fronts to the long channel walls [21]. Results of preliminary visualization experiments, performed in our cell, confirmed this statement. The visualization was done using helium-filled soap bubbles and a laser light sheet. The prevalent structure we observed at different Ra was a double roll with a strong upflow or downflow in the middle of the cell. The observed flow is sketched in Fig. 1. Based on these observations we selected one position exactly between the two convection rolls and the other one above the middle of one convection roll. The focus of our study is on the comparison of the data of both measurements positions. In Table I we give a short overview of the results of four previous studies where the temperature field, and in particular the scaling of the rms temperature fluctuations $\sigma(z)$ in the mixing layer, as well as the thickness of the thermal boundary layer δ_{th}, were investigated. The first study was performed by Belmonte *et al.* in a cubic cell with compressed gases at $\mathrm{Pr} = 0.7$ [4]. For $\mathrm{Ra} > 2 \times 10^7$ the results led to a power law dependence of the form $\delta_{th} = \mathrm{Ra}^{\gamma}$ with $\gamma = -0.29$. The analysis was done using

TABLE I. Summary of previous experimental results: Scaling properties of the distribution of rms temperature fluctuations $\sigma(z)$ in the mixing layer and the thickness of the thermal boundary layer δ_{th}.

Reference	Working fluid and geometry	Ra	$\sigma(z)$	$\delta_{th} \sim \mathrm{Ra}^{\gamma}$
Belmonte *et al.* [4]	Water, cubic cell	1.1×10^{9}	$\sigma\sim z^{-0.8}$, $\sigma\sim\ln(z)$	$\gamma=-0.29$
	SF_6, cubic cell	$4\times10^{5}<\mathrm{Ra}<10^{11}$	$\sigma\sim z^{-0.72}$, $\sigma\sim\ln(z)$	
Lui and Xia [5]	Water, cylindrical cell	$10^{8}<\mathrm{Ra}<10^{10}$		$-0.33\leqslant\gamma\leqslant-0.29$
Fernandes and Adrian [7]	Water, rectangular cell	$10^{7}<\mathrm{Ra}<10^{9}$	$\sigma\sim\ln(z)$	
Du Puits *et al.* [14]	Air, cylindric cell	$10^{9}<\mathrm{Ra}<10^{12}$	$\sigma\sim z^{-0.44<\beta<-0.3}$	$\gamma=-0.25$

the extrapolation method and will be described in Sec. II D. Another study was performed by Lui and Xia in a cylindrical cell filled with water [5]. They confirmed the dependence $\delta_{th}=\mathrm{Ra}^{-0.29}$ just for the measurement in the central axis of the cylinder. Toward the cylinder wall the exponent γ increased and approached the "classical" value $\gamma=-0.33$. Yet another work that is relevant to our own investigations was done by Fernandes and Adrian with emphasis on the rms scaling in the mixing layer; this will be discussed in Sec. III D. The latest and most extensive study about Rayleigh-Bénard convection with emphasis on the structure of thermal boundary layer was recently published by du Puits *et al.* for a large-scale cylindrical cell [14].

The paper is organized as follows. In Sec. II we describe our experimental method and procedures. This section consists of four subsections where we specify the experimental setup, the measurement system, the signal processing, and the determination of thermal boundary layer thicknesses, respectively. The experimental results are presented in Sec. III, which is divided into four subsections. Section III A discusses the long-time temperature series. Secs. III B and III C discuss the properties and statistical analysis of temperature profiles. We summarize our analysis in the discussion about boundary layer thickness in Sec. III D and conclude our study in Sec. IV.

II. EXPERIMENTAL METHOD AND PROCEDURES

A. Experimental setup

The configuration of the Rayleigh-Bénard cell used in the present experiment is shown in Fig. 2(a). The working fluid is air. The cell is a rectangular box with 2.5 m length, 0.5 m width, and 0.5 m height. The box is heated from below (cooled from above) by means of 37-mm-thick water-heated (water-cooled) plates. The plates are made of aluminum. The copper pipes, located inside the plates, have a diameter of 20 mm. In order to ensure a low level of temperature nonuniformities along the plates the distances between the pipes in the plate are only 30 mm. Two separate water circulation systems with pumps provide the temperature control of both plates. The heating plate can be heated up to 100 °C. This value is limited by the boiling temperature of water and the temperature stability of the Perspex walls. The minimum acceptable temperature of the cooling plate is 10 °C, because of condensation effects that take place below 10 °C. The heating and cooling apparatuses have an accuracy of temperature adjustment of ±0.1 K. The construction of the cooling and heating plates ensures a temperature distribution inhomogeneity of ±0.1 °C on the surface of the plates. This uniformity is comparable to that in Ref. [14]. The temperature distribution within both plates is monitored by 40 Pt-100 (platinum resistance thermometer, at temperature $T_0=0$, the resistance $R_0=100\ \Omega$) temperature probes.

The sidewalls of the cell have a thickness of 8 mm and are made of Perspex. This transparent material allows optical access to the cell for future optical flow measurement. In order to reduce heat losses between the cell and the environment, the side walls are isolated with Styrodur. An insulating layer of 180 mm thickness was found to be sufficient to minimize heat losses through the walls. With the described temperature interval from the minimal cooling plate temperature of 10 °C and maximal heating plate temperature of 90 °C, and the distance between the plates $h=0.5$ m, we can cover a range of Rayleigh numbers from $\mathrm{Ra}\approx6\times10^{7}$ up to $\mathrm{Ra}\approx6\times10^{8}$. We define our Cartesian coordinate system as follows. We place the origin at the center of the lower surface of the cooling plate. The x axis is parallel to the long side of the upper plate, and the z axis is oriented downward. Our central measurement position is $X_c=-50$ mm, whereas our peripheral measurement position is $X_p=650$ mm [Fig. 2(a)].

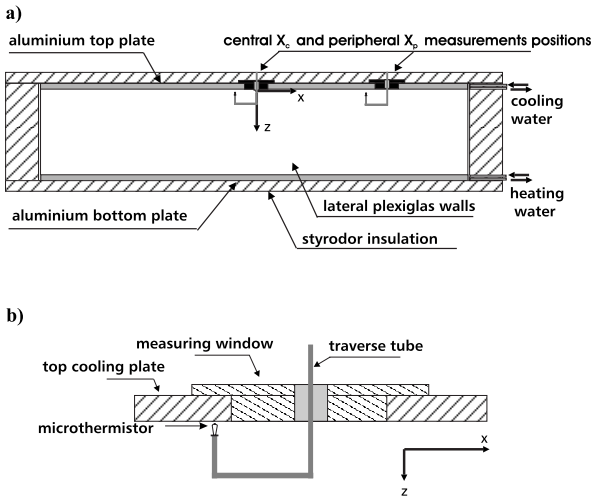

FIG. 2. Schematic of the Rayleigh-Bénard cell with central X_c and peripheral X_p measurement positions (cut along the longitudinal axis of the cell) (a); schematic of the thermistor probe positioning for both measurement positions (b).

B. Measurement system

To investigate the local temperature profiles, a sensor system based on a glass-encapsuled negative temperature coefficient (NTC) microthermistor is used. The microthermistor has a diameter of 120 μm. The thermistor is mounted on a 4-mm-thick support and a small transistor case, as shown in Fig. 2(b). Between the pins of the transistor case the sensor is fixed by a 20-μm-thick wire. The sensor can be moved between $z=0.07$ mm and $z=150$ mm with a one-dimensional (1D) traverse system. The smallest step of the sensor displacement is 10 μm. The smallest distance between the sensor and plate wall corresponds to one-half of the thermistor diameter. A fundamental problem is the correct adjustment of the sensor at the starting position. The distance between the plate and the sensor has to be as small as possible, but without any electrical contact with the plate surface. Otherwise the contact short-circuits and creates signal errors. During the adjustment the sensor image was zoomed ten times by a digital camera and displayed on the monitor. The resolution of the monitor allows an adjustment of the sensor with an accuracy of 50 μm. In order to avoid measurement errors due to a self-heating effect, a very low current is used for the thermistor operation. The resistance variance from the thermistor is amplified by a resistance bridge with an internal dc voltage source. The bridge performs two functions in the measurement, namely, the transformation of the resistance variance from the thermistor to a voltage signal and an amplification by a factor of 100. The output voltage of the bridge is measured by a digital multimeter HP3458. This device has a maximum sampling rate of 333 s^{-1} and a resolution of six digits. The whole measuring system is controlled by a personal computer with LABVIEW software. The voltage signal from the multimeter is converted into the temperature value and all sampled data are saved on hard disk. The traverse system with a step motor are operated automatically by a personal computer. The measurement interval is located in the range $0.07<z<150$ mm distance from the cooling plate and is sampled at 34 nonequidistant positions with 10 μm steps in the vicinity of the plate. The usual measuring time for each position was 1.5 h with a sampling rate of 200 s^{-1}, resulting in $k=1\,080\,000$ temperature values for one position. As a result 34 temperature series $T_i(z)$ with $1 \leqslant i \leqslant k$ represent the raw data for the temperature profile. The total measurement time for one complete profile amounts to 50 h. All long-time errors caused by remaining environmental influences are largely excluded by a random selection of the measurement positions.

C. Profiles

Due to the vigorous heat transport processes in turbulent Rayleigh-Bénard convection, the mean temperature sufficiently far away from the walls is often approximately equal to

$$T_b = T_c + \frac{\Delta T}{2}. \tag{11}$$

Even though this is not always the case in our experiment, probably due to large-scale flow structures, we use this nominal bulk temperature to normalize our temperature fields. Our primary measurement data are time-series of temperature which we denote as $T_i(z)$. This abbreviation stands for the ith value of temperature taken from the sensor that is located at position z. For the dimensionless representation of data we use the quantity $\Theta_i(z)$ defined as

$$\Theta_i(z) = \frac{T_i(z) - T_c}{T_b - T_c}. \tag{12}$$

The profiles of the normalized mean temperature $\Theta(z)$ are calculated from the time series $\Theta_i(z)$ by

$$\Theta(z) = \frac{1}{K}\sum_{i=1}^{K} \Theta_i(z). \tag{13}$$

We further characterize the temperature field by calculating the profiles $\Sigma(z)$ of the standard deviation. These quantities have the dimension kelvin and are defined as

$$\Sigma(z) = \left(\frac{1}{K}\sum_{i=1}^{K} [T_i(z) - T(z)]^2 \right)^{1/2}. \tag{14}$$

The standard deviation enables us to calculate the nondimensional rms temperature fluctuations defined by

$$\sigma(z) = \frac{\Sigma(z)}{\Delta T}. \tag{15}$$

This quantity will later be used for the characterization of the flow in the mixing zone and the definition of one of several boundary layer thicknesses. The profiles $s(z)$ and $k(z)$ of skewness and kurtosis, respectively, give us additional information about the flow structure and provide additional possibilities to define the boundary layer thicknesses. The skewness $s(z)$ is calculated by

$$s(z) = \frac{1}{K}\frac{\sum_{i=1}^{K} [T_i(z) - T(z)]^3}{\Sigma^3}, \tag{16}$$

whereas the kurtosis $k(z)$ is defined as

$$k(z) = \frac{1}{K}\frac{\sum_{i=1}^{K} [T_i(z) - T(z)]^4}{\Sigma^4}. \tag{17}$$

D. Boundary layer thicknesses

The concept of a boundary layer plays a key role in turbulent thermal convection. It is desirable to characterize the structure of the thermal boundary layer by a small number of quantities that can be extracted from the profiles $\Theta(z)$, $\sigma(z)$, $s(z)$, and $k(z)$ defined in the previous section. These quantities, which we refer to as boundary layer thicknesses, will be defined next. Belmonte *et al.* [4] and many other investigators define the thickness δ_{th} of the thermal boundary layer as

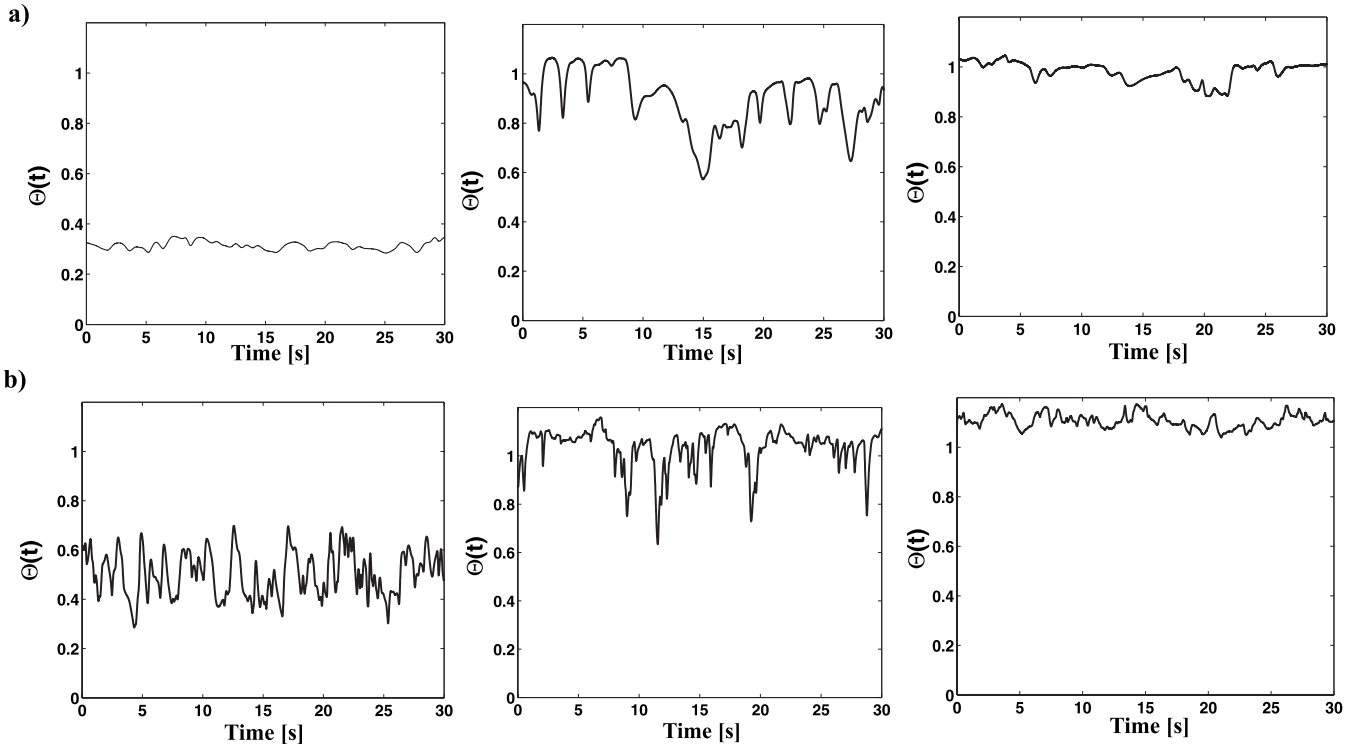

FIG. 3. Temperature time series from position X_c at three different z (from left to right, $z=1.4$, 16, and 150 mm), for $\mathrm{Ra}=5.6\times10^7$ (a) and $\mathrm{Ra}=6\times10^8$ (b).

$$\delta_{th}=\left(\left.\frac{d\Theta}{dz}\right|_{z=0}\right)^{-1}. \tag{18}$$

This definition tacitly assumes $\Theta(z)|_{z=0}=0$ (isothermal plates). The boundary layer thickness so defined can be interpreted as the distance from the wall at which the extrapolation of the linear portion of the mean temperature profile equals the bulk temperature. Belmonte *et al.* [4] found a power law dependence of the boundary layer thickness δ_{th} on Ra which is given in Table I. The quantity δ_{th} cannot be used in our experiment because our measured temperature profiles do not obey $\Theta(0)=0$. This effect has already been observed in other Rayleigh-Bénard experiments with air [14] and will be explained in detail in the discussion in Sec. III B. A second boundary layer thickness can be defined using the maximum of the rms profile $\sigma(z)$. The mathematical description of this definition is

$$\delta_\sigma=\{z:\sigma(z)=\max\}. \tag{19}$$

Belmonte *et al.* [4] found that for $\mathrm{Ra}>2\times10^7$ this maximum is located exactly at δ_{th}. The quantity δ_σ will be used below to characterize our boundary layers.

Two other boundary layer length scales based on the profiles of skewness and kurtosis will be applied. They were already discussed by du Puits *et al.* [14]. The first one is defined by the point where the skewness of the temperature fluctuations vanishes, whereas the second one is the point at which the kurtosis is equal to that of a signal with Gaussian distribution. In mathematical terms,

$$\delta_s=\{z:s(z)=0\},\quad \delta_k=\{z:k(z)=3\}. \tag{20}$$

The length scales so defined will be discussed in detail in Sec. III C.

III. EXPERIMENTAL RESULTS

A. Time series of temperature

We start to describe the experimental results with a discussion of temperature time series. As mentioned earlier, long-time series at 34 different positions were measured for each Ra. Due to the high sampling rate, we can observe all fluctuations even on the smallest scale and get detailed information about the temperature field at every measurement position. In the example in Fig. 3 the high temporal resolution of our measurement can be seen. For comparison the results of two different Ra, namely, $\mathrm{Ra}=5.6\times10^7$ [Fig. 3(a)] and $\mathrm{Ra}=6\times10^8$ [Fig. 3(b)] are shown. The normalized temperature is plotted over a time interval of 30 s. The value $\Theta(t)=0$ corresponds to the temperature of the cooling plate and the value $\Theta(t)=1$ corresponds to the idealized bulk temperature. The changing of the temperature signal character along the z axis is a clear illustration of the three-layer model proposed by Castaing *et al.* [11]. First we look at the results of higher Ra, which are shown in Fig. 3(b). In the first diagram ($z=1.4$ mm) the fluctuations are comparatively large and are distributed nearly symmetrically around the mean value. The influences of the wall and the mean flow are thus approximately balanced and the measurement point is probably located at the boundary between the mixing and diffusive lay-

ers [11]. By contrast, the temperature signal from the same measurement point at a lower Ra [shown in Fig. 3(a)] is smooth and shows a behavior that is characteristic of a temperature field in the diffusive layer. In the next diagram, corresponding to a distance of $z=16$ mm, the temperature is close to the bulk temperature but shows strong negative spikes. This indicates that cold plumes in the mixing zone cause a strongly nonisothermal flow. We observed the same plumes at lower Ra, with the difference that the motion of the plumes was much slower. For $z=150$ mm the fluctuations of the temperature signal are found to be small at both values of Ra and represent a relatively constant bulk temperature in the strongly mixed core. Notice that in Fig. 3(b) the temperature for $z=150$ mm is slightly above the nominal bulk temperature, probably due to upflow of hot air.

B. Profiles of mean temperature

We now turn to the discussion of the mean temperature profiles. Because the height of our cell is constant, we plot these profiles as a function of the nondimensional distance from the cooling plate z/h. When the profiles are plotted using linear scales for Θ and z/h, we observe the well-known shape in our measurements, as expected. The temperatures increase very quickly within the boundary layer below the cooling plate and converge toward a nearly constant value in the bulk. This representation of the profiles is not shown here. An important characteristic of the profile should, however, be mentioned. If the temperature profile is extrapolated from the measurement position closest to the wall ($z=70$ μm) to the wall ($z=0$), we obtain a nonzero value of $\Theta(0)$. The higher Ra, the stronger the deviation. This effect can be interpreted at as a consequence of the finite size of the thermistor whose diameter is approximately 125 μm. In the immediate vicinity of the cooling plate a high-temperature gradient occurs. Because the thermal conductivity of the sensor is much higher than of air, the vertical heat flux through the sensor caused the measured temperature to be a local average of the true temperature gradient. The same phenomenon was already observed by du Puits *et al.* [14] in experiments with air at higher Rayleigh numbers. However, our main conclusions regarding the structure of the boundary layers outside the diffusive layer are unaffected by this finite-sensor-size effect.

The question whether the temperature profiles outside the diffusive region obey a power law or a logarithmic law was already mentioned in the introduction of this paper. We answer it by using the so-called diagnostic functions $\Gamma(z)=d(\ln\Theta)/d(\ln z)$ and $\Xi(z)=d\Theta/d(\ln z)$, which were already used by Zanoun and Durst [19] for the analysis of velocity profiles in shear flows. Constancy of Γ indicates a power law profile whereas constancy of Ξ is a characteristic of a logarithmic profile. An analysis of the diagnostic functions for our temperature profiles led to the result that for the overwhelming majority of cases a power law provides a better approximation than a logarithmic law. We therefore present our profiles in Figs. 4 and 5 in a double-logarithmic form. The inset of Fig. 5 shows the behavior of the power-law diagnostic function for selected Rayleigh numbers.

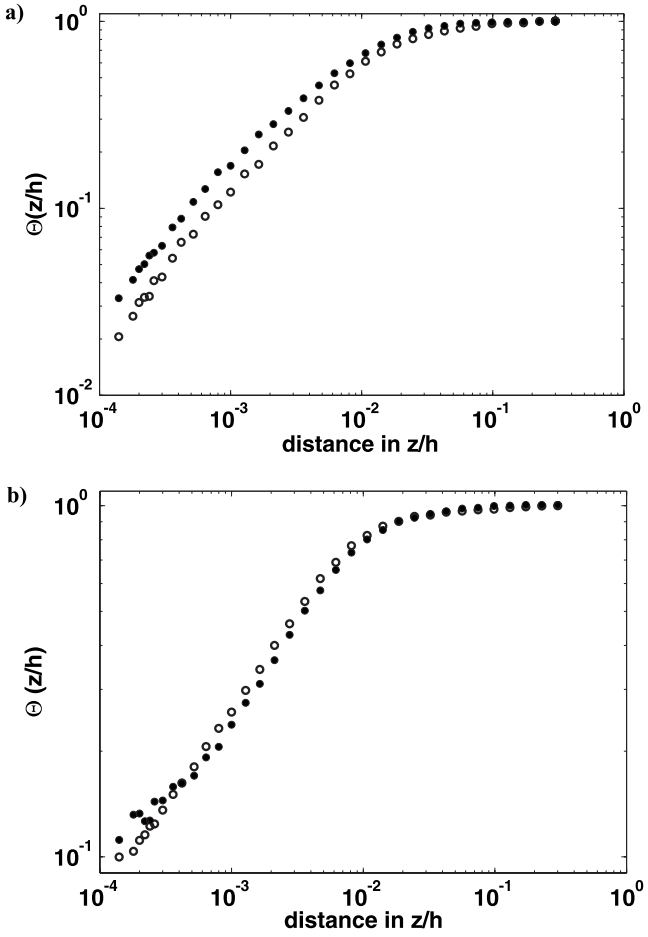

FIG. 4. Comparison of the temperature profiles at two different measurement positions X_c (○) and X_p (●) for Ra$=1.5\times10^8$ (a) and 4.7×10^8 (b).

In Fig. 4 we compare the temperature profiles for equal Ra measured at the central and peripheral positions. It can be seen that in all cases there are regions in which the temperature profiles (in double-logarithmic representation) are linear, which indicates power law behavior. It can further be seen

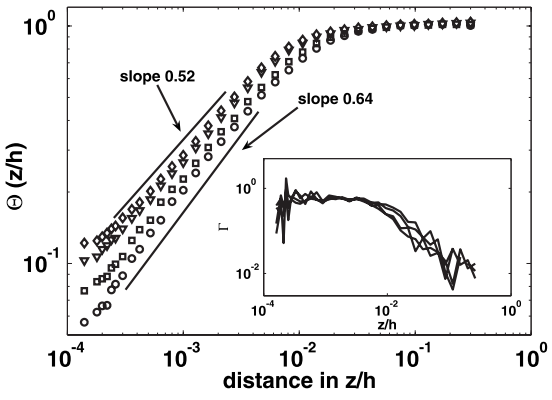

FIG. 5. Temperature profiles at the peripheral measurement position X_p for different Rayleigh numbers: Ra=(○) 2.3×10^8, (□) 3.7×10^8, (▽) 4.7×10^8, and (◇) 6×10^8 (slopes are shown for the lowest and highest Rayleigh numbers). Inset: power law diagnostic function Γ for the displayed profiles.

TABLE II. Summary of scaling exponents for the profiles of the mean temperature and of the rms temperature fluctuations as obtained by the measurements at positions X_c and X_p.

Position	Ra	α	β
X_c	6×10^8	0.57	−0.43
	4.7×10^8	0.56	−0.55
	3.7×10^8	0.56	−0.56
	2.3×10^8	0.51	−0.58
	1.5×10^8	0.57	−0.44
	8.2×10^7	0.56	−0.58
	5.6×10^7	0.60	−0.63
X_p	6×10^8	0.52	−0.44
	4.7×10^8	0.54	−0.44
	3.7×10^8	0.58	−0.64
	2.3×10^8	0.64	−0.67
	1.5×10^8	0.68	−0.67
	8.4×10^7	0.62	−0.73
	5.7×10^7	0.60	−0.77

that the curves for the different measurement positions can exhibit considerable differences as in Fig. 4(a) for Ra=1.5×10^8, but can also be quite similar as in Fig. 4(b) for Ra=4.7×10^8. In spite of a comprehensive analysis of the differences between the mean temperatures at the central and peripheral measurement positions we have found no systematic dependence of the disparity of the profiles on Ra. A similar statement applies to the profiles of the higher-order moments, discussed in the next section. We propose that a possible reason for this fact comes from the shape of the large-scale flow structure. The central measurement position is located at a stagnation point (in case of upflow in the middle of the box) or in a converging flow (in case of downflow in the middle of the box), whereas the peripheral position is in a region of persistent mean flow as shown in the sketch in Fig. 1. This explains why we observe a higher variability of the statistical properties of the temperature field at the central measurement position. Let us now analyze how the profiles evolve with increasing Rayleigh number. In Fig. 5 four temperature profiles, measured at the position X_p, are shown. When Ra increases, the slope of the profiles decreases. This implies that the curvature of the profiles (in linear representation) rises. The slopes for the profiles at Ra=2.3×10^8 and 6×10^8 are also given in Fig. 5. The measured values of the scaling exponents α [appearing in $\Theta\sim z^{\alpha}$; cf. Eq. (10)] for both measurement series are summarized in Table II. In our results from the central measurement position X_c the value of α changes without any distinct tendency. By contrast, at the peripheral position X_p we observe a systematic decrease of α when Ra is increased from Ra=1.5×10^8 to 6×10^8. This shows that the scaling properties of the mean temperature profile can vary significantly in convection with one large aspect ratio.

Before discussing the profiles of higher-order moments, a comment on the behavior of the temperature profile far away from the wall is in order. In our measurement the temperature profiles reach the bulk with a temperature which is not exactly equal to the bulk temperature, i.e., $\Theta\neq1$ for $z/d\rightarrow1/2$. A similar effect, which is likely the reason for this observation, has been earlier observed in a cubic cell [23,24]. An in-depth analysis of this phenomenon was performed by Gluckmann *et al.* [23] in a small water cell at $7\times10^6<$Ra

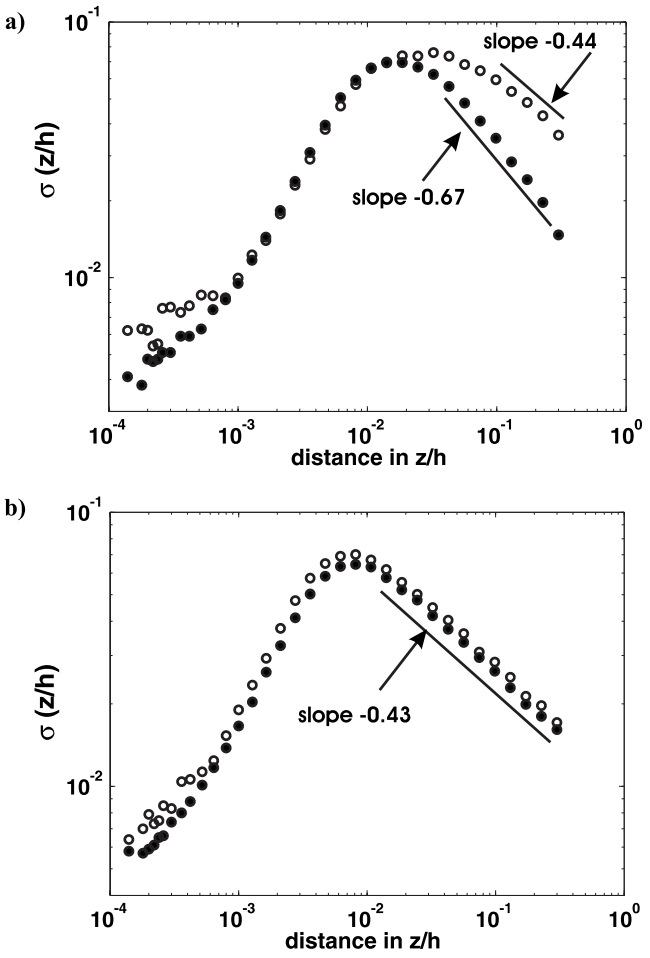

FIG. 6. Comparison of the profiles of the rms temperature fluctuations $\sigma(z/h)$ measured at two different measurement positions X_c (○) and X_p (●) for Ra=1.5×10^8 (a) and 6×10^8 (b).

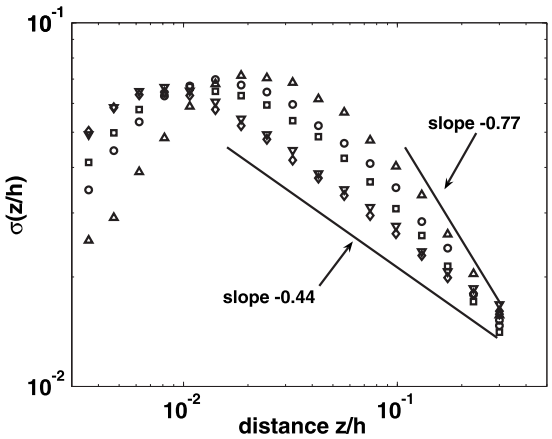

FIG. 7. Profiles of rms temperature fluctuations at position X_p; Ra=8.2×10^7 (△), 2.3×10^8 (○), 3.7×10^8 (□), 4.7×10^8 (▽), and 6×10^8 (◇).

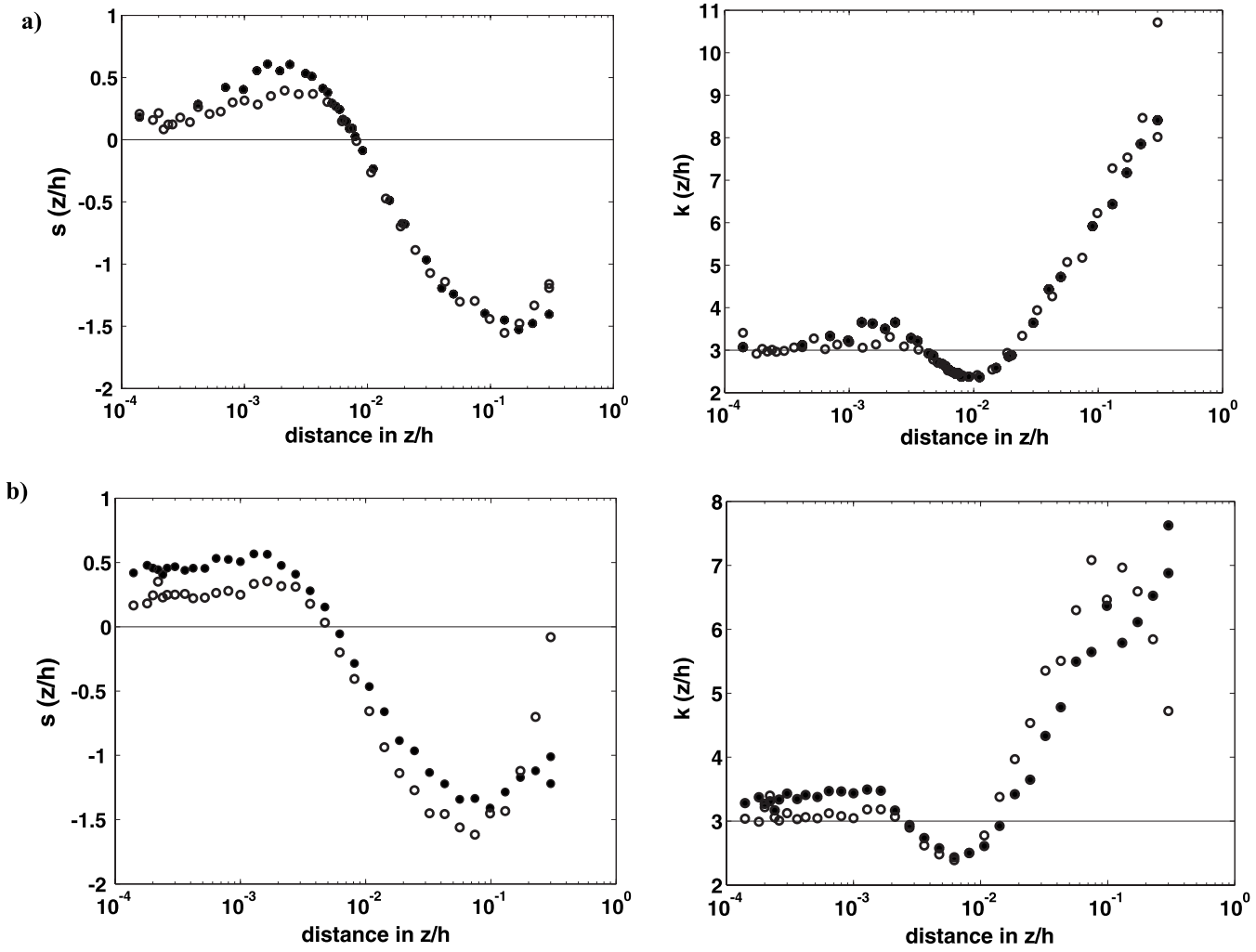

FIG. 8. Comparison of the skewness and kurtosis profiles at two different measurement positions X_c (○) and X_p (●) for Ra=2.3 $\times 10^8$ (a) and 4.7×10^8 (b).

$<3\times 10^8$, using liquid crystal imaging for temperature field visualization. The results show that the temperature in the upper half of the cell (near the cooling plate) tends to be higher than the mean temperature of the cell, and that the lower half (near the heating plate) is cooler than the average. This so-called inversion of the mean temperature can be caused by the shape of the large-scale flow patterns and the direction of the flow field. As already explained in Sec. I, the dominant flow structure in our cell was a double roll with a strong upflow or downflow in the middle of the cell. With the changing in the flow field direction, temperature can be distorted, resulting in inversion.

C. Profiles of higher-order moments

There are three phenomenological theories for the shape of $\sigma(z)$ inside the mixing layer, namely, Priestley's [13] classical prediction

$$\sigma \sim z^{-1/3}, \tag{21}$$

the so-called λ I theory (Castaing *et al.* [11]; Deardorff and Willis [8])

$$\sigma \sim z^{-1/2}, \tag{22}$$

as well as the λ II theory [11] (see also Fernandes and Adrian [7]), which predicts

$$\sigma \sim \ln(z). \tag{23}$$

The first two predictions are particular cases of the more general relation $\sigma \sim z^{\beta}$. We are interested in the question of whether one of these relations describes our experimental data.

In Fig. 6 we compare the profiles of $\sigma(z/h)$ for both measurement positions at equal Ra and see quite different behaviors. In particular, the z position of the maximum and the slope of the decrease are important. In Fig. 6(a) the comparison for profiles at Ra=1.5×10^8 is shown. We can see noticeable differences between them. They have different slopes and the locations of their maxima are at different values of z. In Fig. 6(b) $\sigma(z)$ measured at Ra=6×10^8 are shown. The shape of the profile is virtually the same. A systematic analysis of differences between the σ profiles for both measurement positions did not show any systematic dependence on Ra. In Table II we list the complete set of all

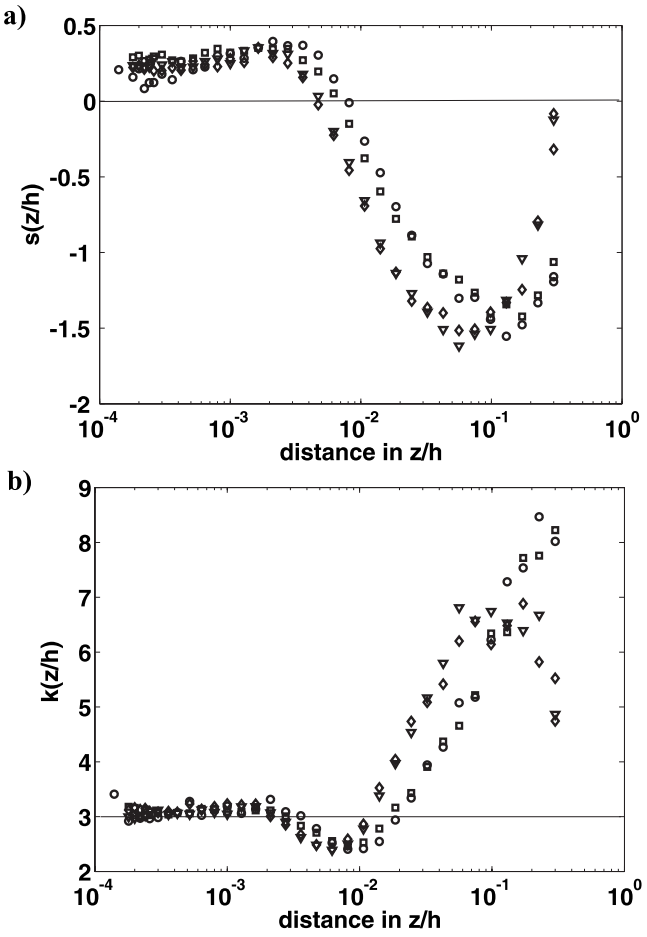

FIG. 9. Profiles of skewness $s(z/h)$ (a) and kurtosis $k(z/h)$ (b) for four different values of Ra at position X_p: Ra=2.3×10^8 (○), 3.7×10^8 (□), 4.7×10^8 (▽), and 6×10^8 (◇).

experimentally determined scaling exponents β. The λ I theory predicts a value of $\beta=-0.5$. We observed this value just for a part of our range of Ra. This range is different for the two measurement positions. At position X_p, β reaches the vicinity of −0.5 just for two values of Ra, namely, Ra=4.7×10^8 and 6×10^8. For X_c the range of Ra where $\beta\approx-0.5$ holds is much larger, namely, from Ra=1.5×10^8 up to Ra=6×10^8. A semilogarithmic view of rms profiles for five values of Ra from 8.2×10^7 up to 6×10^8, measured at position X_p, is shown in Fig. 7. We focus our observations on the part of the profiles that begins after the maximum of profiles is reached. In this example we can clearly see that with increasing Ra the slope decreases. The results for both measurement positions are shown in Table II. The data show that, if the decay of the rms temperature fluctuations obeys a power law, the exponent is closer to the prediction of the λ I theory than to Priestley's formula. It should be mentioned, that the decrease of some rms profiles for Ra below 10^8 are also consistent with a logarithmic function $\sigma\sim\ln(z)$ as predicted by the λ II theory. Hence our experiments do not provide an unambiguous answer as to whether a logarithmic or a power law decay of the rms temperature fluctuations holds.

The skewness reflects the asymmetry of the sampled data distribution around the mean value. Figure 8 shows the profile of the skewness at the central and peripheral measurement positions. Near the wall the value of the skewness is small and positive. For higher z there is a point where it vanishes, in which case the distribution of the sampled data is symmetrical. The symmetric fluctuations at the point where $s(z)=0$ show that the influences of the cooling plate and the bulk are counterbalanced in some respect and compensate each other. This position is equal to the length scale δ_s which has been defined in Sec. II. In the following part of the profile, the skewness decreases strongly under the influence of the cold plumes in the mixing zone. After reaching the minimum, it returns to the value $s(z)=0$. In this case symmetrical fluctuations are caused by a perfectly mixed fluid in the core. After reaching $s(z)=0$ the skewness profile becomes positive again under the influence of hot plumes ascending from the heating plate. Because of the limitation of our measurement range in the z direction, we were not able to reach the value $s(z)=0$ in the core, but we can clearly observe the tendency of skewness to become zero for $z\rightarrow h/2$.

The kurtosis is a measure of the "peakedness" of the probability distribution of a real-valued random variable, in our case the temperature. The kurtosis profiles plotted in Fig. 8 show two different kinds of behavior depending on whether one is close to the wall or not. In the first case, the near-wall region, the profile values fluctuated weakly around the value $k(z)=3$. Distributions with $k(z)=3$ are called mesokurtic, one case being the Gaussian distribution. In the $k(z)=3$ position we define also the boundary layer length scale δ_k. In the second region, after reaching the minimum, the kurtosis increases. In Fig. 8 we compare profiles of skewness $s(z)$ and kurtosis $k(z)$. Similar to the behavior of the rms temperature

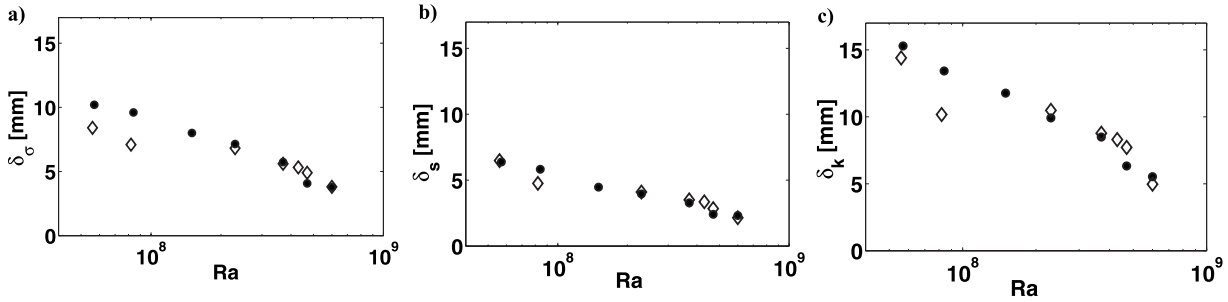

FIG. 10. Boundary layer length scales versus Rayleigh number for the measurement positions X_c (◇) and X_p (●), determined using rms (a), skewness (b) and kurtosis (c).

TABLE III. Values of the boundary layer thicknesses at different x positions calculated from the profiles of rms temperature fluctuations, skewness, and kurtosis.

x position	Ra	δ_σ (mm)	δ_s (mm)	δ_k (mm)
X_c	6×10^8	3.8	2.15	4.97
	4.7×10^8	4.9	2.84	7.71
	4.3×10^8	5.32	3.36	8.3
	3.7×10^8	5.6	3.51	8.77
	2.3×10^8	6.82	4.1	10.48
	8.2×10^7	7.09	4.76	10.17
	5.6×10^7	8.4	6.49	14.4
X_p	6×10^8	3.78	2.32	5.53
	4.7×10^8	4.07	2.41	6.33
	3.7×10^8	5.73	3.28	8.49
	2.3×10^8	7.14	3.96	9.92
	1.5×10^8	8	4.47	11.77
	8.4×10^7	9.6	5.83	13.42
	5.7×10^7	10.2	6.38	15.29

fluctuations, there are cases of agreement as in Fig. 8(a) as well as disagreement as in Fig. 8(b).

We can see for the measurement at $\mathrm{Ra}=4.7\times10^8$ [see Fig. 8(b)] that, in the region close to the wall, $s(z)$ and $k(z)$ are closer to the Gaussian values 0 and 3, respectively, for position X_c than for X_p. The data from X_p in the near-wall area differ from a Gaussian distribution and are probably affected by the strong large-scale flow.

In Fig. 9(a) the profiles of skewness $s(z)$ for four different values of Ra measured at X_p are compared. In our results $s(z)$ reaches a minimum in the range $-1.4<s<-1.8$ for all investigated values of Ra. These results are comparable with the results of Belmonte *et al.*, who obtain a skewness minimum in the range $-1.6<s<-1.8$ for $10^7<\mathrm{Ra}<10^9$ [4]. We also have observed that the magnitude and position of the extremum of skewness, caused by the maximum of signal asymmetry, hardly changes with Ra.

In Fig. 9(b) kurtosis profiles $k(z)$ measured at four different values of Ra are compared. At $\mathrm{Ra}=6\times10^8$ and 4.7×10^8 the kurtosis attains the maximum of $k\approx6.5$. The maximum of the kurtosis indicates the fewest coincident data distributions in this area. It indicates intensive disintegration of cold plumes, which impact the flow. After reaching the maximum, the profile returns toward the Gaussian value $k=3$ in the core.

At lower Ra the maximum of $k(z)$ moves toward the cell center and cannot be measured because of the limited z range in our measurements.

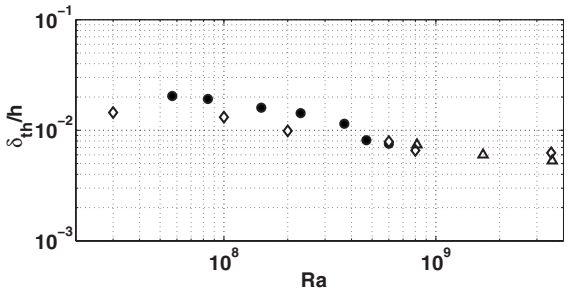

FIG. 11. Comparison of boundary layer length scales with previous experiments: Belmonte *et al.* (◇), du Puits *et al.* (△), and present work (●). All length scales are made nondimensional using the height of the relevant cell.

D. Boundary layer length scales

Using the definitions introduced in Sec. II D we compute the values of the boundary layer length scales for all investigated values of Ra. The results are summarized in Table III. Let us compare the results for the two measurement positions and discuss how the boundary layer length scales depend on Ra.

The boundary layer length scales in both measurement positions change continuously for the investigated range of Rayleigh numbers. Generally, the width of the boundary layer is reduced with the increase of Ra.

The boundary layer length scales are summarized in Fig. 10 as functions of Ra. A significant difference between the results from X_c and X_p can be recognized immediately. At the peripheral position X_p we observe a monotonic and continuous decrease of all three length scales, which can be approximated with a power law $\delta_{\sigma,s,k}=C_{1,2,3}\times\mathrm{Ra}^{\gamma_{\sigma,s,k}}$. The scaling exponents are summarized in Table IV. It can be inferred from this table that the exponents are nearly identical as their values are between −0.42 and −0.44. In contrast to the observations at the peripheral measurement position, the boundary layer length scales at the position X_c show a considerable scatter and their dependence on Ra cannot be described by a simple function. The difference of the properties of the thermal boundary layers between our two measurement positions is one of the main findings of the present paper. One possible explanation could be based on the shape of the large-scale structures that we observed by optical flow visualization. The prevalent convective flow structure consists of two convection rolls, as sketched in Fig. 1. X_c is located at the center of the cell. In this area, between two convection rolls, we observe an intensive upflow or downflow leading to the formation of stagnation points close to the plates. The unstable flow structure in this area might cause strong variability of the statistical properties, which were used for determination of $\delta_{\sigma,s,k}$. By contrast, X_p is lo-

TABLE IV. Scaling of the boundary layer thickness.

x position	$\delta_\sigma=C_1\times\mathrm{Ra}^{\gamma_\sigma}$	$\delta_s=C_2\times\mathrm{Ra}^{\gamma_s}$	$\delta_k=C_3\times\mathrm{Ra}^{\gamma_k}$
X_p	$\delta_\sigma=23468\times\mathrm{Ra}^{-0.43}$	$\delta_s=17814\times\mathrm{Ra}^{-0.44}$	$\delta_k=26972\times\mathrm{Ra}^{-0.42}$

cated above the middle of a roll structure. The stable character of the flow gives rise to well-defined statistical properties and good agreement between different scales. In Fig. 11 we compare our results for δ_σ from position X_p with δ_{th} from Belmonte *et al.* [4] and δ_σ measured by du Puits *et al.* [14]. Thereby δ_{th}/h is the boundary layer normalized to the height of the relevant cell. Despite the differences in the geometry—a small cubic cell in [4], a large-scale cylindrical cell with aspect ratio close to unity in [14]—we can see a good agreement of the results.

IV. CONCLUSION

We have studied the profiles of mean temperature, rms temperature fluctuations, skewness, and kurtosis in turbulent Rayleigh-Bénard convection in an elongated rectangular cell. Despite our modest Rayleigh numbers as compared to some experiments listed in Table I, our work probes turbulent Rayleigh-Bénard convection by means of temperature profiles with very high spatial and temporal resolution. It is particular importance that the measurement was performed at two distinctive positions in the cell with a special geometry, which had not been studied before to our knowledge. The main result of our work is the observation that the properties of the thermal boundary layers can vary significantly along the long side of the cell. We have further demonstrated that the dependence of the mean temperature on the vertical coordinate can be approximated by a power law with an exponent α that decreases with increasing Rayleigh number, in agreement with recent findings of du Puits *et al.* [14] at higher Rayleigh numbers. Our analysis of the decay of the rms temperature fluctuations with increasing distance from the wall did not lead to a clear answer as to whether this decay obeys a power law, as suggested by Priestley, or a logarithmic law. Our observations show that the structure of the large-scale flow has a significant influence on the properties of the thermal boundary layer. We believe that velocity measurements are necessary to shed new light on the structure of the large-scale flow.

ACKNOWLEDGMENTS

The authors thank the Helmholtz Association of the German Research Centers for financial support. We are grateful to R. du Puits for helpful discussions and to V. Mitschunas and H. Hoppe for their technical support.

[1] S. Grossmann and D. Lohse, J. Fluid Mech. **407**, 27 (2000).
[2] J. J. Niemela, L. Skrbek, K. R. Sreenivasan, and R. J. Donelly, Nature (London) **404**, 837 (2000).
[3] F. Chilla, S. Ciliberto, C. Innocenti, and E. Pampaloni, Nuovo Cimento Soc. Ital. Fis., D **15**, 1229 (1993).
[4] A. Belmonte, A. Tilgner, and A. Libchaber, Phys. Rev. E **50**, 269 (1994).
[5] S.-L. Lui and K.-Q Xia, Phys. Rev. E **57**, 5494 (1998).
[6] D. B. Thomas and A. A. Townsend, J. Fluid Mech. **2**, 473 (1957).
[7] R. L. J. Fernandes and R. J. Adrian, Exp. Therm. Fluid Sci. **26**, 355 (2002).
[8] J. W. Deardorff and G. E. Willis, J. Fluid Mech. **28**, 675 (1967).
[9] A. A. Townsend, J. Fluid Mech. **5**, 209 (1958).
[10] U. Mueller and P. Ehrhard, *Freie Konvektion und Waermeuebertragung* (C.F. Mueller Verlag, Heidelberg, 1999).
[11] B. Castaing, G. Gunaratne, F. Heslot, L. Kadanoff, A. Libchaber, S. Thomae, X.-Z. Wu, S. Zaleski, and G.-M. Zanetti, J. Fluid Mech. **204**, 1 (1989).
[12] X.-L. Qiu and P. Tong, Phys. Rev. Lett. **87**, 094501 (2001).
[13] C. H. B. Priestley, Aust. J. Phys. **7**, 176 (1954).
[14] R. du Puits, C. Resagk, and A. Thess, J. Fluid Mech. **572**, 231 (2007).
[15] M. Hoelling and H. Herwig, J. Fluid Mech. **541**, 383 (2005).
[16] L. Prandtl, Beitr. Phys. Atmos. **19**, 188 (1932).
[17] L. D. Landau and E. M. Lifschitz, *Fluid Mechanics*, Course of Theoretical Physics Vol. 6 (Pergamon Press, Oxford, 1959).
[18] G. I. Barenblatt, J. Fluid Mech. **248**, 513 (1993).
[19] E.-S. Zanoun and F. Durst, Phys. Fluids **15**, 3079 (2003).
[20] M. H. Buschmann and M. Gad-el-Hak, AIAA J. **41**, 40 (2003).
[21] A. V. Getling, *Rayleigh-Bénard Convection, Structure and Dynamics* (World Scientific, Singapore, 1998).
[22] H. Schlichting and K. Gersten, *Boundary Layer Theory* (Springer Verlag, Berlin, 2000).
[23] B. J. Gluckmann, H. Willaime, and J. P. Gollub, Phys. Fluids A **5**, 647 (1993).
[24] A. Tilgner, A. Belmonte, and A. Libchaber, Phys. Rev. E **47**, R2253 (1994).